RESEARCH ARTICLE

Unraveling Mixtures: A Novel Underdetermined Blind Source Separation Approach via Sparse Component Analysis

YANYANG LI [1,2], **JINDONG WANG** [1], **HAIYANG ZHAO** [1], **CHANG WANG** [1], **AND ZHICHAO MA** [1]

[1]College of Mechanical Science and Engineering, Northeast Petroleum University, Daqing 163318, China
[2]College of Civil Engineering and Water Conservancy, Heilongjiang Bayi Agricultural University, Daqing 163319, China

Corresponding author: Haiyang Zhao (zhaohaiyang2003@126.com)

ABSTRACT Underdetermined blind source separation (UBSS) is a critical technique in the field of intelligent mechanical operation and maintenance that allows for the disentanglement of source signals from their mixtures without the need for prior knowledge or extensive sensor information. The accuracy of source signal recovery depends on the estimation of the mixing matrix. To promote sparsity in source signals, we employed methods such as sparse representation and sparse component analysis. Traditional approaches, such as the Short-Time Fourier Transform (STFT), often suffer from limited time-frequency resolution, motivating the adoption of the Synchronous Extraction Transformation (SET) algorithm, which closely approximates the ideal time-frequency transform. SET significantly enhances the sparsity of the signals, thus facilitating the separation of the mixed signals. In the context of sparse component analysis, we introduce an improved density peaks clustering (DPC) method that successfully resolves source number estimation issues and robustly eliminates outliers. This improvement leads to a more accurate mixing matrix estimation. To determine the cluster centers, we employed K-means clustering, further refining our source separation process. In summary, our study presents an innovative approach that combines the Synchronous Extraction Transformation (SET) with 'an improved density peaks clustering (DPC)' method and K-means for mixing matrix estimation. Source signal recovery was achieved using the shortest-path algorithm. Extensive simulations and experiments validate the effectiveness of the method, outperforming the traditional techniques. When applied to rolling bearing fault diagnosis, the proposed approach effectively separates complex signals and accurately identifies the fault characteristic frequencies.

INDEX TERMS Underdetermined blind source separation, synchronous extraction algorithm, K-means, sparse component analysis, complex mechanical signals.

I. INTRODUCTION

The primary task in mechanical fault diagnosis is to extract the characteristic frequency of the vibration signal to determine a fault. The blind source separation technique is commonly and extensively utilized in fault diagnosis owing to its advantages, such as ease of application, quick com-

The associate editor coordinating the review of this manuscript and approving it for publication was Yiming Tang.

putation, and lack of requirement for prior knowledge [1], [2]. In an ideal scenario, the overdetermined blind source separation model refers to a situation in which there are more sensors (m) than source signals (n). Conversely, when the number of sensors (m) matches exactly with the number of source signals (n), it is known as a positive definite blind source separation model. However, in practical situations, an underdetermined blind source separation model arises when there are fewer sensors (m) than the number of

source signals (*n*). According to existing literature, research approaches for blind source separation techniques include Independent Component Analysis (ICA), convolution mixed models, and Sparse Component Analysis (SCA). ICA is commonly applied in overdetermined and positive definite models, although its effectiveness is limited by the assumption of independence [3], [4], [5]. The Convolution mixed model attempts to solve the nonlinear model for recovering the source signals, but its complexity in theory and computational difficulty render it a technology that has not yet been fully developed [6], [7], [8]. In constrast, SCA is a classical technique for underdetermined blind source separation, specifically designed to address the underdetermination issue by requiring the source signals to exhibit sparsity, thereby enabling the separation of signals from the mixed signal [9], [10].

Sparse Component Analysis (SCA) has witnessed significant evolution in the field of signal processing, leading to various refinements and adaptations over the years. In its early stages, SCA was rooted in the "source disjointness" assumption (WDO) [11]. Researchers have assumed that each observed point in the time-frequency domain is exclusively associated with a single source. This foundational concept treats source separation as a clustering problem, in which the goal is to segregate sources based on their unique characteristics. As research progressed, the source sparsity assumption was relaxed, giving rise to a methodology now known as SCA [12], [13], [14]. This relaxation allowed multiple sources to be concurrently active at the same time-frequency points. However, the focus remained on identifying regions in which only one source actively contributed to the observed signal. This transition expanded the flexibility of SCA, making it more suitable for real-world scenarios in which strict source disjointness may not hold. With further development, the SCA was extended to accommodate cases with more than two observations. Researchers discovered that source separation was still feasible, provided that the number of active sources at each time-frequency point remained strictly less than the number of observations [15], [16]. This adaptation has enabled the application of SCA in situations involving a broader array of observations and sources. A noteworthy refinement was the transition from identifying single-source zone works to pinpoint single-source points, and the present study adopts this single-source point assumption [17]. SCA has been applied not only in the realm of instantaneously mixed signals but also in scenarios such as anechoic environments, convolutive mixtures [18],and even nonlinear mixtures [19], [20], [21]. Furthermore, SCA methods have been successfully integrated with source localization techniques, enabling more accurate estimations of the number and locations of the sources. In some cases, adhoc clustering methods have been proposed, as outlined in [22], to effectively count and locate sources. Finally, SCA methods bear similarities with Convex Non-Negative Matrix Factorization (NMF) and Volume-Constrained NMF. While

Convex NMF has primarily been employed in hyperspectral unmixing and Volume-Constrained NMF in audio signal processing, ongoing efforts aim to extend the applicability of SCA to hyperspectral unmixing [23] and Convex Volume-Constrained NMF to audio domains [24]. Certain SCA methods have also been adapted to address scenarios with missing data entries, as explored in [25].

For SCA to be applied well, its two main steps, that is, sparse representation and sparse component analysis, must be performed successfully. Sparse representation refers to the process of converting a signal into the time-frequency domain through time-frequency analysis (TFA) to enhance signal sparsity. However, classical time-frequency analysis methods suffer from low time-frequency resolution, for example, the short-time Fourier transform (STFT) is sensitive to bounded perturbations of Gaussian white noise and sparsity is difficult to increase owing to the Heisenberg uncertainty principle. Meanwhile, the Wigner-Ville distribution (WVD) has the disadvantage of long computation time and difficult reconstruction owing to the presence of unexpected cross terms [26].

Various clustering algorithms have emerged in the context of sparse component analysis, each with distinctive strengths and limitations. As a density-based clustering method, DPC offers distinct advantages, including the ability to identify clusters with uneven densities. However, the DPC presents several challenges and drawbacks. First, it relies on distance metrics and density estimation and requires careful selection of appropriate parameters and kernel functions [27]. Incorrect parameter choices may result in inaccurate clustering. In addition, DPC exhibits relatively high time complexity, particularly in the case of large-scale datasets, where algorithm efficiency requires improvement [28]. Finally, DPC tends to form convex clusters, posing challenges in recognizing non-convex clusters [29]. On the other hand, K-means clustering is a classic clustering method renowned for its simplicity and efficiency, making it the preferred choice in many applications. Nevertheless, K-means clustering also has its limitations. First, prior knowledge of the number of clusters is necessary, which can be challenging to determine in certain scenarios. Second, in the presence of noisy data points, K-means clustering is sensitive to the selection of initial cluster centers, resulting in unstable outcomes [30], [31], [32], [33].

The primary drawback of SCA-based methods is their inferior estimation performance in the presence of noise. Furthermore, the application of SCA-based approaches is challenging when dealing with unknown source number. In this section, we propose a new Underdetermined blind source separation (UBSS) analysis method to overcome the shortcomings in SCA, which enhances the accuracy of the mixed matrix estimation.The main achievements of this study can be summarized as follows:

1. Innovative Holistic Approach: This study introduces a novel blind source separation method that integrates

multiple key techniques, including enhanced density peaks clustering (DPC) and K-means clustering, along with the utilization of Synchronous Extraction Transformation (SET). The innovation lies in the ability of this holistic approach not only to address the challenge of source signal estimation but also to effectively eliminate outliers, thereby significantly improving the accuracy of the mixing matrix estimation.

2. Refined Details: Our approach incorporates an improved DPC (IDPC), which, through the optimization of the decision graph and introduction of standardization techniques, successfully resolves the source number estimation problem. This refinement enhances the clustering accuracy while making the algorithm more robust against outliers. Furthermore, by combining K-means clustering with IDPC, we enhanced the precision of mixing matrix estimation. These detailed improvements enable our method to handle complex signal mixtures better, ultimately enhancing the effectiveness of signal separation.

3. Enhanced Sparsity with SET: In contrast to the conventional Short-Time Fourier Transform (STFT), we adopt the Synchronous Extraction Transformation (SET), which offers distinct advantages in terms of signal sparsity. The application of SET further enhanced the signal sparsity, providing substantial assistance for the separation of mixed signals. This innovative decision improves signal separation accuracy, particularly in cases involving signal overlap and complexity.

4. Simulation and Experimental Validation: Through extensive simulations and experiments, we thoroughly validate the efficacy of the proposed method. Compared with traditional methods, our approach exhibits superior performance in terms of mixing matrix estimation and signal separation. Experimental results demonstrate that our method is highly effective in separating complex signals and accurately identifying fault characteristic frequencies, ultimately enhancing the system performance.

Concerning the aforementioned principles, the content of this study is structured as follows: Section II provides comprehensive details on the SCA topic; Section III elaborates on the new UBSS method; Section IV includes experimental validation, and Section V concludes the study.

II. PRINCIPLE OF SCA
A. MOTIVATION OF SCA
In practical applications, it is often observed that the mixed signals obtained from sensors fail to meet the sparsity requirements. For example, three signals $\mathbf{S(t)}$ are combined into two signals $\mathbf{X(t)}$ through arbitrary matrix $\mathbf{A}$.

$$X(t) = A \times S(t) \qquad (1)$$

Figure 1(a) depicts the image of $\mathbf{X(t)}$ in the time domain, demonstrating spatially irregular scattering characteristics. On the other hand, Figure 1(b) portrays the image of $\mathbf{X(t)}$ in the time-frequency domain, revealing the evident presence of three straight lines. In this transformed domain, clustering algorithms were used to obtain the direction vectors of
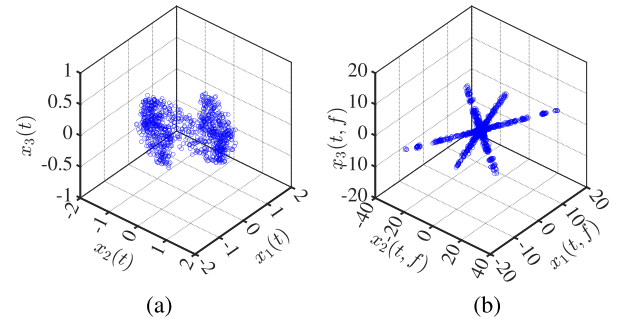

FIGURE 1. Scatter plot in (a)time domain; and (b) time-frequency domain.

straight lines, represented by column vectors of the mixing matrices. Once both the mixed signals and mixing matrices are identified, least-squares methods can be employed to recover source signals from underdetermined equations with sparse solutions. However, the clustering characteristics of mixed signals are not easily discernible owing to the presence of randomly distributed noise.

A single-source point identification method is commonly employed to enhance signal sparsity before estimating the mixing matrix. Term "single-source point" refers to a point in a sparse domain that contains only one source. In (2), $\mathbf{X(t)}$= $[x_1(t), x_2(t), \ldots, x_m(t)]^T$ represents m observation signals collected by m sensors, $\mathbf{S(t)}$= $[s_1(t), s_2(t), \ldots, s_n(t)]^T$ represents n statistically independent source signals, $\mathbf{A}$ represents the mixing matrix of the unknown $m \times n(m < n)$; which can be written as (2):

$$\begin{bmatrix} x_1(t) \\ x_2(t) \\ \vdots \\ x_m(t) \end{bmatrix} = \begin{bmatrix} a_{11} & a_{12} & \cdots & a_{1n} \\ a_{21} & a_{22} & \cdots & a_{2n} \\ \vdots & \vdots & \ddots & \vdots \\ a_{m1} & a_{m2} & \cdots & a_{mn} \end{bmatrix} \begin{bmatrix} s_1(t) \\ s_2(t) \\ \vdots \\ s_n(t) \end{bmatrix} \qquad (2)$$

Converting (2) in the time-frequency domain yields (3).

$$\begin{bmatrix} x_1(t,f) \\ x_2(t,f) \\ \vdots \\ x_m(t,f) \end{bmatrix} = \begin{bmatrix} a_{11} & a_{12} & \cdots & a_{1n} \\ a_{21} & a_{22} & \cdots & a_{2n} \\ \vdots & \vdots & \ddots & \vdots \\ a_{m1} & a_{m2} & \cdots & a_{mn} \end{bmatrix} \begin{bmatrix} s_1(t,f) \\ s_2(t,f) \\ \vdots \\ s_n(t,f) \end{bmatrix} \qquad (3)$$

In the above equation, $x(t,f), s(t,f)$ are the corresponding time-frequency coefficients. Assuming that the time-frequency point (t_k, f_k) is a single-source point, and only the source signals s_i are activated, that is $s_i(t_k, f_k)$, the following relation is established.

$$\begin{bmatrix} x_1(t_k,f_k) \\ x_2(t_k,f_k) \\ \vdots \\ x_m((t_k,f_k) \end{bmatrix} = \begin{bmatrix} a_{1i} \\ a_{2i} \\ \vdots \\ a_{mi} \end{bmatrix} \begin{bmatrix} s_i(t_k,f_k) \end{bmatrix} \qquad (4)$$

Taking the real part of both sides of the equation as in (5),

$$
\begin{bmatrix} R(x_1(t_k, f_k)) \\ R(x_2(t_k, f_k)) \\ \vdots \\ R(x_m((t_k, f_k)) \end{bmatrix} = \begin{bmatrix} a_{1i} \\ a_{2i} \\ \vdots \\ a_{mi} \end{bmatrix} \begin{bmatrix} R(s_i(t_k, f_k)) \end{bmatrix} \tag{5}
$$

Taking the imaginary part of both sides of the equation, as in Equation (8):

$$
\begin{bmatrix} I(x_1(t_k, f_k)) \\ I(x_2(t_k, f_k)) \\ \vdots \\ I(x_m((t_k, f_k)) \end{bmatrix} = \begin{bmatrix} a_{1i} \\ a_{2i} \\ \vdots \\ a_{mi} \end{bmatrix} \begin{bmatrix} I(s_i(t_k, f_k)) \end{bmatrix} \tag{6}
$$

In scenarios where the time-frequency points align with a solitary source point, the proportion of the real components of signals $x_i(t_k, f_k)$ and $x_j(t_k, f_k)$, is equivalent to the ratio of the imaginary components of $x_i(t_k, f_k)$ and $x_j(t_k, f_k)$. These similarities align with the vector direction of the mixing matrix, as indicated by Eqs.(7) and (8).

$$
\frac{R(x_i(t_k, f_k))}{R(x_j(t_k, f_k))} = \frac{a_{ii}}{a_{ji}} \tag{7}
$$

$$
\frac{I(x_i(t_k, f_k))}{I(x_j(t_k, f_k))} = \frac{a_{ii}}{a_{ji}} \tag{8}
$$

However, the zero point is difficult to realize owing to noise; therefore, the noise must be eliminated by choosing an appropriate error parameter as shown in (9).

$$
\left| \frac{R(x_i(t_k, f_k))}{R(x_j(t_k, f_k))} - \frac{I(x_i(t_k, f_k))}{I(x_j(t_k, f_k))} \right| = \lambda \tag{9}
$$

B. SPARSE REPRESENTATION METHOD

To date, the most recent methods include synchronous transformation (SST) [34], [35], [36] and synchronous extraction transformation (SET). Specifically, based on the STFT results, SST compresses all time-frequency (TF) coefficients into an instantaneous frequency (IF) trajectory and removes the most contaminated TF energy, greatly enhancing the new TF representation [37], [38]. The SET algorithm is a post-processing method for STFT that effectively eliminates transient energy points in time-frequency coefficients, bringing it closer to the ideal time-frequency transformation rather than the general approach. Taking the harmonic signal $s(u) = A \cdot e^{iw_0 u}$ as an example, the principle of SET is analyzed in detail. First, STFT is applied; the Gauss window is generally used, and according to the length of the signal, the window length is selected, and the time-frequency representation of the harmonic signal is shown in (10):

$$
G(t, w) = \int_{-\infty}^{\infty} g(u - t) \cdot s(u) \cdot e^{-iwu} du \tag{10}
$$

where $g(u - t)$ represents a window function, u represents time, t represents time shift, w represents the frequency. From Parseval's identity perspective, equation (10) can be written

as (11):

$$
G(t, w) = \frac{1}{2\pi} \int_{-\infty}^{\infty} \hat{s}(\zeta) \cdot (\hat{g}(\zeta))^* d\zeta \tag{11}
$$

where $\hat{s}(\zeta)$ represents the Fourier transform of the harmonic signal $s(u)$; $(\hat{g}(\zeta))^*$ represents the conjugate complex of the Fourier transforms $g(u)$. By expanding (11), we can get (12):

$$
G(t, w) = \frac{1}{2\pi} \int_{-\infty}^{\infty} \hat{s}(\zeta) \cdot \hat{g}(\omega - \zeta) \cdot e^{i\zeta t} d\zeta \tag{12}
$$

Harmonic signal $s(u)$ is applied to the STFT transformation, as shown in (13).

$$
\hat{s}(w) = 2\pi A \cdot \delta(\omega - \omega_0) \tag{13}
$$

Take (13) in (12), then get (14):

$$
G_e(t, \omega) = A \cdot \hat{g}(\omega - \omega_0) \cdot e^{i\omega_0 t} \tag{14}
$$

By calculation of the derivative of time, we can get (15):

$$
\partial_t G_e(t, \omega) = G_e(t, \omega) \cdot i \cdot \omega_0 \tag{15}
$$

According to (15), the instantaneous frequency of the signal at different time-frequency points can be estimated, as shown in (16):

$$
\omega_0(t, \omega) = -i \cdot \frac{\partial_t G_e(t, \omega)}{G_e(t, \omega)} \tag{16}
$$

The time-frequency coefficients which are the instantaneous frequencies obtained from the STFT spectrum are extracted from the above equations.

$$
Te(t, \omega) = G_e(t, \omega) \cdot \delta(\omega - \omega_0(t, \omega)) \tag{17}
$$

where δ is a synchronous extraction operator, expressed as (18):

$$
\delta(\omega - \omega_0(t, \omega)) = \begin{cases} 1, \omega = \omega_0 \\ 0, \omega \neq \omega_0 \end{cases} \tag{18}
$$

In the following, we employ two simulation experiments to illustrate that the time-frequency resolution and sparsity of the signal are significantly improved after the SST processing.

Simulation 1: let us consider the function $f(x) = \sin(500\pi t)$. A comparison between the Short-Time Fourier Transform (STFT) and Synchrosqueezing Transform (SST) is shown in Figure 2. Figure 2(a) shows the waveform of the signal, while Figure 2(b) illustrates the theoretical instantaneous frequency. Figures 2(c) and 2(d) present the time-frequency representation of the signal using STFT and SST respectively. Comparing Figure 2(c) to Figure 2(b), it becomes apparent that the energy of the signal is dispersed owing to the window effects in STFT. On the other hand, Figure 2(d) demonstrates that SST achieves a superior concentration of time-frequency information by reassigning TF coefficients from their original positions to their gravity center along the frequency direction. This leads to sparser TF coefficients in SST than in STFT.
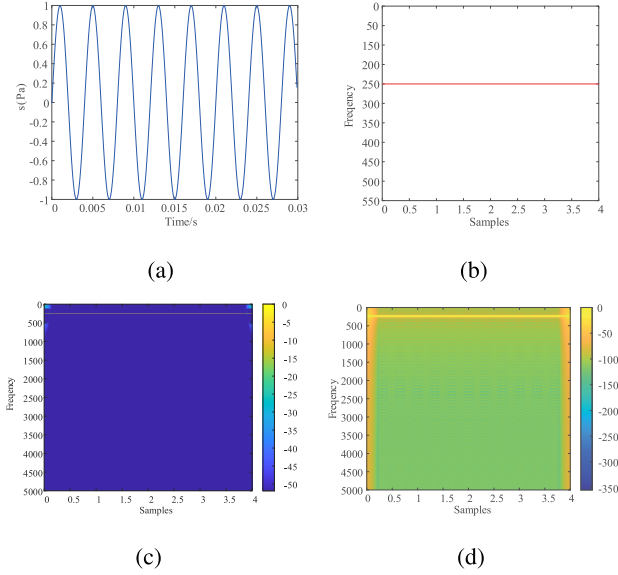
FIGURE 2. SST schematic diagram. (a) Time domain signal; (b) theorized instant frequency; (c) TF expression of the STFT; (d) TF expression of the SST.
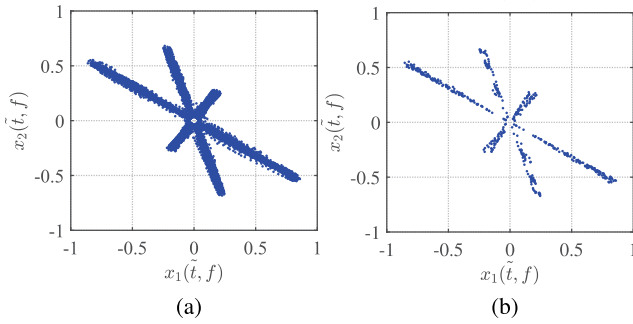

FIGURE 3. TF domain diagram of mixed signals: (a) after STFT conversion; (b) after SET conversion.

Simulation 2: Two distinct methods were employed to demonstrate the difference in sparsity between SET and STFT when converting signals from the time domain to the frequency domain. The mixed signals **X** are transformed into the time-frequency domain using STFT, resulting in the dispersion diagram shown in Figure 3(a) after detecting a single source point. This diagram revealed noise points surrounding the lines that significantly affected the accuracy of estimating the mixed matrix. In contrast, utilizing SET to convert mixed signals into the TF domain produced a dispersion diagram, as shown in Figure 3(b) after detecting a single source point. Comparing Figures 3(a) and 3(b), there is a decrease in the number of noise points observed, a linear enhancement of the mixed signal, and a clear TF point with no overlap. SET is better than STFT in terms of time-frequency sparsity.

By mapping normalization, Figure 4(a) was compared with Figure 4(b), and owing to the inadequacy of the STFT algorithm, the clustering in Figure 4(a) is concatenated into
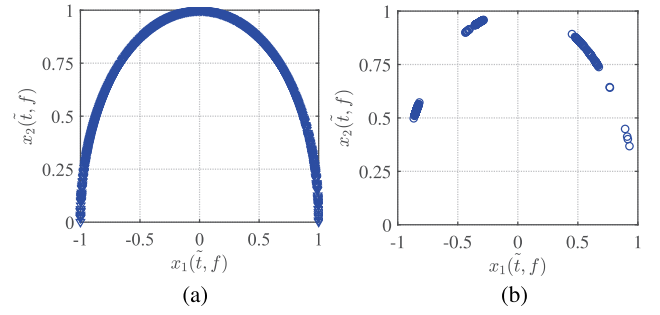

FIGURE 4. TF domain mapping normalization: (a) after STFT conversion; (b) after SET conversion.

a line after normalization with no classification effect which affects the efficiency and accuracy of the clustering method. The number of clusters in Figure 4(b) is obvious and presents three classes.

Based on the aforementioned analyses of the two simulations, it is evident that a higher level of sparsity leads to improved clustering. In additional, in the SET process, numerous interference points are eliminated, and signal preprocessing in this stage significantly enhances the accuracy of the estimation matrix.

C. SPARSE COMPONENT ANALYSIS

The density peaks clustering (DPC) algorithm, which was published in the prestigious US journal Science in 2014 [27], presents a pioneering approach to clustering by utilizing density. DPC stands out for its ability to perform clustering without the need for iterative processes or additional parameters [39]. It diverges from the well-established K-means algorithm by eliminating the prerequisite of empirically determining the number of classes. Moreover, DPC excels in efficiently identifying non-spherical clusters and effectively removing noise points [40], [41]. The core concept of the algorithm is based on two assumptions.

Assumption 1: The central point of a cluster has a local density greater than that of its neighboring points, and there is a relatively large distance between the central points of a cluster.

Assumption 2: The group of each sample point was divided by calculating its local density and offset distance.

The outlined procedures of the DPC clustering algorithm are as follows.

Step 1: Calculate the local density ρ_i of each data.

$$\rho_i = \sum_j \chi(d_{ij} - d_c) \tag{19}$$

The local density is calculated from (19) according to the given truncation distance d_c. Typically, each data point has 1-2% of the total number of data points as neighbors. where d_{ij} represents the data point x_i and x_j distance, and in most cases uses the Euclidean distance; d_c represents the truncation distance, generally by artificial setting; and the expression

for χ:

$$\chi(x) = \begin{cases} 1, & x < 0 \\ 0, & x \geq 0 \end{cases} \qquad (20)$$

Step 2: Calculate the offset distance δ_i of high-density point, as shown in Equation (21).

$$\delta_i = \min_{j:\rho_j > \rho_i} (d_{ij}) \qquad (21)$$

The minimum distance from each point to a point above the local density is calculated. The offset distance δ_i signifies the closest distance from any point where the local density exceeds that of data point x_i to data point x_j.

Step 3: The anomalies in the frequency points of the signals observed by DPC identification are eliminated.

After obtaining the cluster centers, we assign each point to the cluster with the highest density in its vicinity, which maintains a certain distance from the data points of other clusters as dc. We then identify the boundary regions of each cluster and partition the data points within the same cluster into two subsets: the cluster core and halo. The former consists of points with larger local densities, whereas the latter consists of smaller points. We computed the average local density for each cluster and used it as a cutoff value to separate the core from the halo. Finally, we detected and removed outliers located in the halo regions of the clusters.

Step 4: The decision diagram is drawn to determine the cluster centers.

When it comes to the selection of the cluster center, the decision graph is a compromise between the two parameters, which takes the local density ρ as the horizontal axis, and the offset distance δ is drawn on the vertical axis. By observing the points with a higher local density and offset distance, when the values of ρ and δ are relatively large, this point is selected at the cluster center.

For cases in which the cluster centers cannot be determined in the decision diagram, a method to determine the number of cluster centers is given in Article [42]: Calculate a final indicator that combines ρ and δ, $\gamma_i = \rho_i \times \delta_i$. The probability of being a cluster center increases with the larger value γ. The parameters γ are arranged in descending order, and multiple data points are selected from the beginning as the clustering centers. However, determining the number of cluster centers can be susceptible to errors.

Consider an example of data categorization. An illustration of the figure below shows that 30 data points in Figure 5 are represented in the scatterplot. Simultaneously, it can be deduced that there are two clustering centers. Additionally, it is worth mentioning that the three data points with numbers 7, 9, and 23 are considered "outliers" in the original dataset because of their large values for the parameters but small values for ρ.

As depicted in Figure 6, data points 2, 18, and 30 are notable for their relatively high double parameter values. The preliminary assessment at this crucial point suggests that there are three clusters is 3, yet this assumption is incorrect.
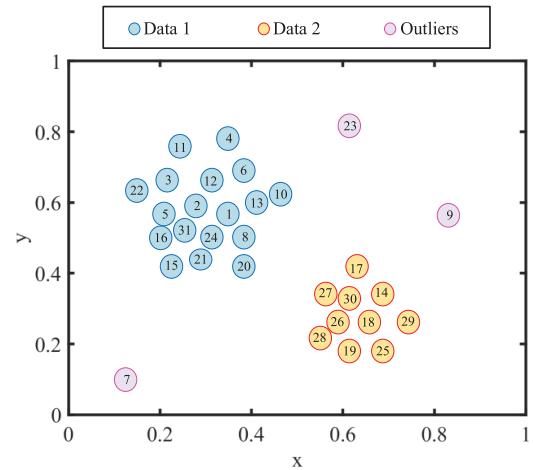

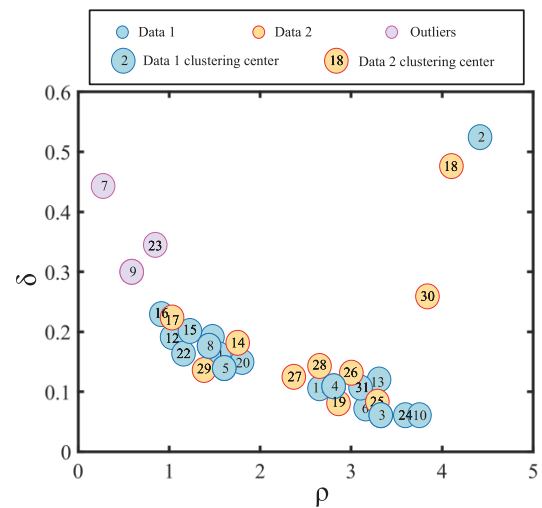**FIGURE 5.** Scatterplot of data.

FIGURE 6. Cluster center qualitative identification map.

Manual selection is combined with subjectivity and uncertainty, disrupting the smooth progression of the algorithm. Attempts to automatically detect centers have proven challenging, sparking the interest of countless scholars. Xu et al. [43] proposed an improved clustering algorithm based on density peaks with the capability of quickly identifying cluster centers. In a similar vein, Hou et al. [44] rely on the relative density relationship to locate cluster centers, thereby minimizing the impact of density kernels. Flores et al. [45] proposed a method that employs the identification of gaps between data points in a one-dimensional version of the decision graph to automatically ascertain cluster centers. Xu et al. [46] employed support vectors to calculate the feedback value between clusters, resulting in clustering outcomes. Despite the various methods mentioned above for promptly detecting appropriate clustering centroids, they often lead to increased algorithmic complexity or parameter adjustments. However, there seems to be limited consideration for simplifying
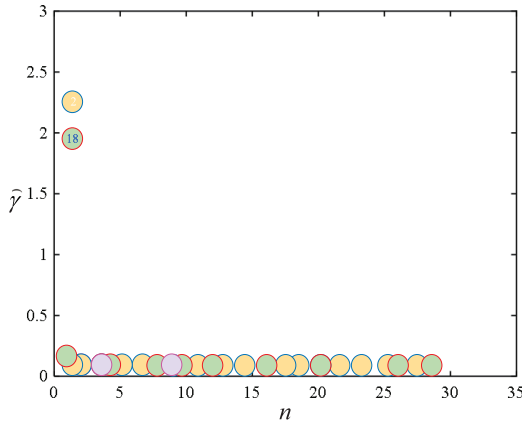
FIGURE 7. The decision graph of IDPC.

the computational process while ensuring a high degree of compliance and integration with the original DPC clustering algorithm.

III. A NOVEL UBSS METHOD

A. THEORY OF THE PROPOSED METHOD
In our research, we leveraged the K-means clustering algorithm as a fundamental tool for sparse component analysis. However, this widely- used algorithm has some inherent limitations. The first challenge we encounter with K-means clustering is the arbitrary initialization of the clustering centers. This issue often leads to suboptimal results because the algorithm can be trapped in the local optima. Additionally, the arbitrary selection of initial centers can significantly increase the computational burden because it requires multiple iterations to find the best solution [47], [48]. The second challenge is related to handling of outliers in the data. K-means is not inherently robust to outliers. When outliers are present in the samples, K-means may mistakenly assign them as data points to the clusters closest to their centers. This misallocation can significantly amplify the clustering errors, ultimately affecting the accuracy of our analysis.

To address these challenges, we introduce an improved methodology that combines the DPC clustering algorithm with the K-means approach. This hybrid method provide a robust and efficient solution. The first step in our approach involves the use of the DPC clustering algorithm, which effectively eliminates outliers from the data. In addition, the DPC algorithm accurately estimates the number of source components, which is crucial for our analysis.

However, the DPC algorithm has its own set of challenges. First, our dataset may not have a uniform size, which can affect the quality of clustering. Second, the magnitude of the values within the data has a substantial influence on data distribution and classification across various classes. The next innovation is the enhanced decision diagram for the DPC clustering algorithm. By normalizing the final indicator, the cluster centers can be screened more effectively, resulting

in improved clustering results. Subsequently, we employed the K-means algorithm to compute the final clustering centers. This enhanced version of IDPC not only provides superior clustering results but also significantly improves the computational efficiency and reduces the overall processing time.

To accurately select clustering centroids from a quantitative analysis perspective, we considered and normalized the two parameters. The formula for the IDPC clustering centroid discrimination is given by (22).

$$\tilde{\gamma}_i = \frac{\rho_i \times \delta_i}{(\rho_{max} \times \delta max)} \qquad (22)$$

In the descending order of $\tilde{\gamma}_i$, the decision diagram effectively distinguishes clustering centers from non-clustering centers. Non-clustering center points form a smooth curve close to the horizontal axis, whereas clustering center points stand out, making them easily identifiable. As illustrated in Figure 7, data points 2 and 18 represent the true center points of the clusters.

In summary, our novel Unmixing-Based Sparse Component Analysis (UBSS) methodology follows a structured approach:

Step 1: Transform the signal from the time domain to the time-frequency domain using Short-Time Fourier Transform (STFT). Then, the instantaneous frequency of the signal is determined by utilizing the phase information obtained from the time-frequency signal through (16). Extract the STFT's time- frequency coefficients at the position of the instantaneous frequency via (17), thus achieving the TF conversion of SET.

Step 2: Preprocess the signal by eliminating low-energy TF points, detecting single-source points, and normalizing the TF points according to (23).

$$T_e(\tilde{t}, \omega) = \frac{T_e(t, \omega)}{\|T_e(t, \omega)\|_2} \times \text{sign}\,(T_e(t, \omega)) \qquad (23)$$

Step 3: The local density is calculated using Equation (19). The offset distance is calculated using (21). The anomalies in the frequency points of the signals observed by DPC identification are eliminated. Calculate the final indicator $\tilde{\gamma}_i$ using the discriminant formula (22) and automatically find the initial clustering centroids using the IDPC decision map.

Step 4: Take the cluster centers as the initial centers of K-means and complete the K-means clustering.

Step 5: Estimate the mixing matrix with the clustering center and recover the source signal using the shortest path method.

The detailed flowchart is depicted in Figure 8.

B. NUMERICAL SIGNAL ANALYSIS
In this section, three simulated signals were constructed to simulate the source signals $s = [s_1, s_2, s_3]^T$ in (24). s_1 is a cosine wave with frequency of f_1 and an initial phase of 10 rad. s_2 is another cosine wave with a frequency f_2 and no specific phase information. In contrast, s_3 is a modulated
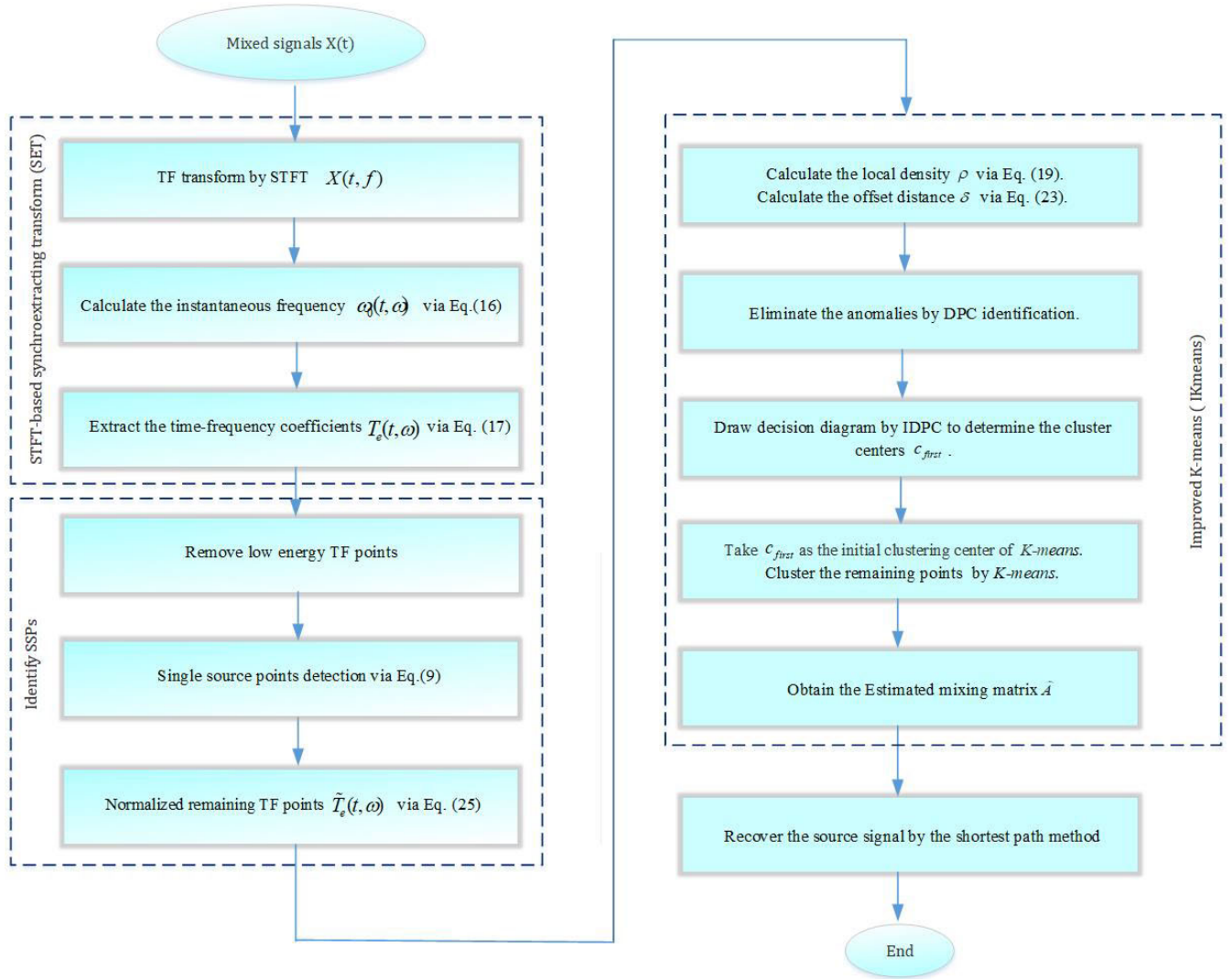
FIGURE 8. The depicted flow chart exemplifies the proposed methodology.

signal that combines two components: a base cosine wave with a frequency of f_b and a phase modulation term. Phase modulation is influenced by a cosine wave with a frequency f_r, and the modulation depth is controlled by the parameter β. The sampling frequency and the number of sampling points are 1024 Hz and 1000, respectively, and Gaussian white noise with mean value 0 and variance 0.1 is added to the mixed signal $\mathbf{X(t)}$ as shown in (24):

$$\begin{cases} s_1 = \cos(2\pi f_1 t + 10) \\ s_2 = 0.7\cos(2\pi f_2 t) \\ s_3 = 0.4\cos[(2\pi f_b t) + \beta\cos(2\pi f_r t)] \end{cases} \quad (24)$$

where $f_1 = 100\text{Hz}$, $f_2 = 220\text{Hz}$, $f_b = 150\text{Hz}$, $f_r = 20\text{Hz}$, $\beta = 0.9$, MATLAB generated a mixed matrix $\mathbf{A}$ randomly as shown in (25):

$$A = \begin{bmatrix} -0.841 & 0.3140 & 0.572 \\ 0.5410 & -0.949 & 0.820 \end{bmatrix} \quad (25)$$

The entire simulation process was used to simulate three signal sources acquired by two sensors in a real noise environment, resulting in two mixed signals. The time domain and frequency domain plots corresponding to the source signals (s_1, s_2, s_3) are shown in Figure 9, and the time domain and frequency domain plots corresponding to the two mixed signals (X_1, X_2) are shown in Figure 10.

$$X(t) = A \times S(t) + 0.1\,N(t) \quad (26)$$

In the frequency spectrum of a mixed signal, there is always a part of the source signal whose corresponding amplitude is too small or too submerged to be recognized. In the spectrum of mixed-signal X_1, the amplitude of $f_1 = 100\text{Hz}$ is the largest, and the amplitudes of the other frequencies are so small that they cannot be recognized. In the spectrum of mixed-signal X_2, the amplitudes of $f_1 = 100\text{Hz}$, $f_3 = 220\text{Hz}$ are larger, and the rest of the frequency amplitude is minimal. Therefore, for
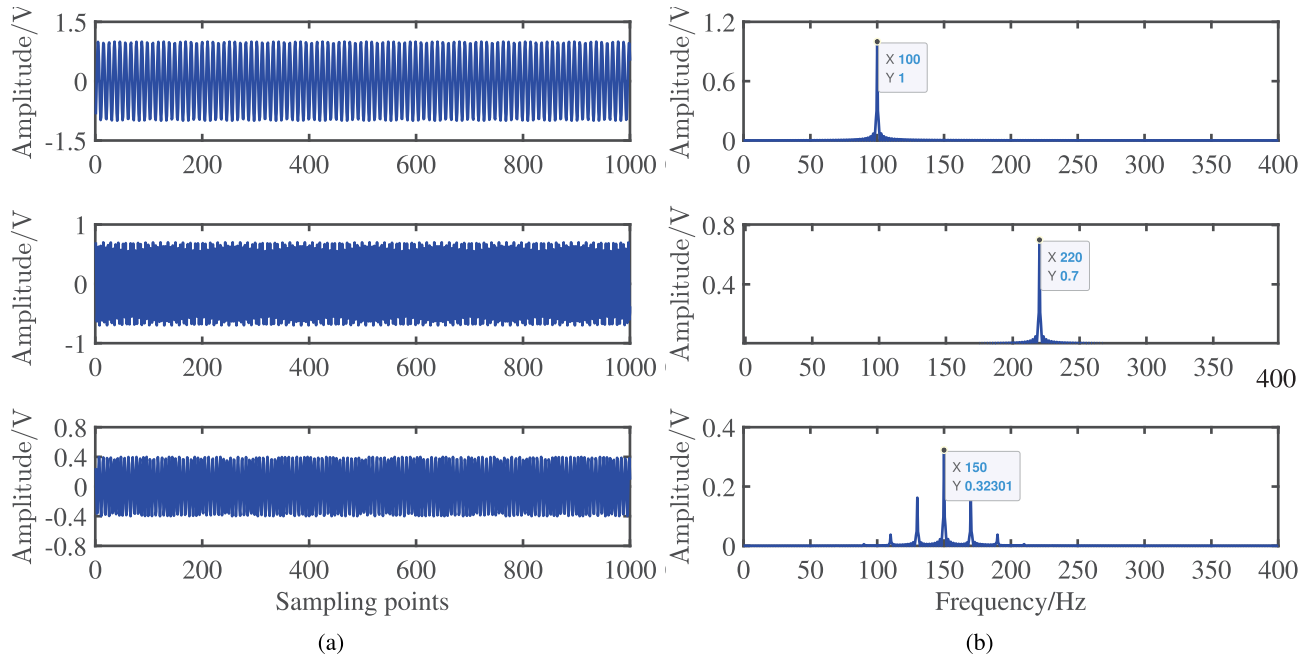
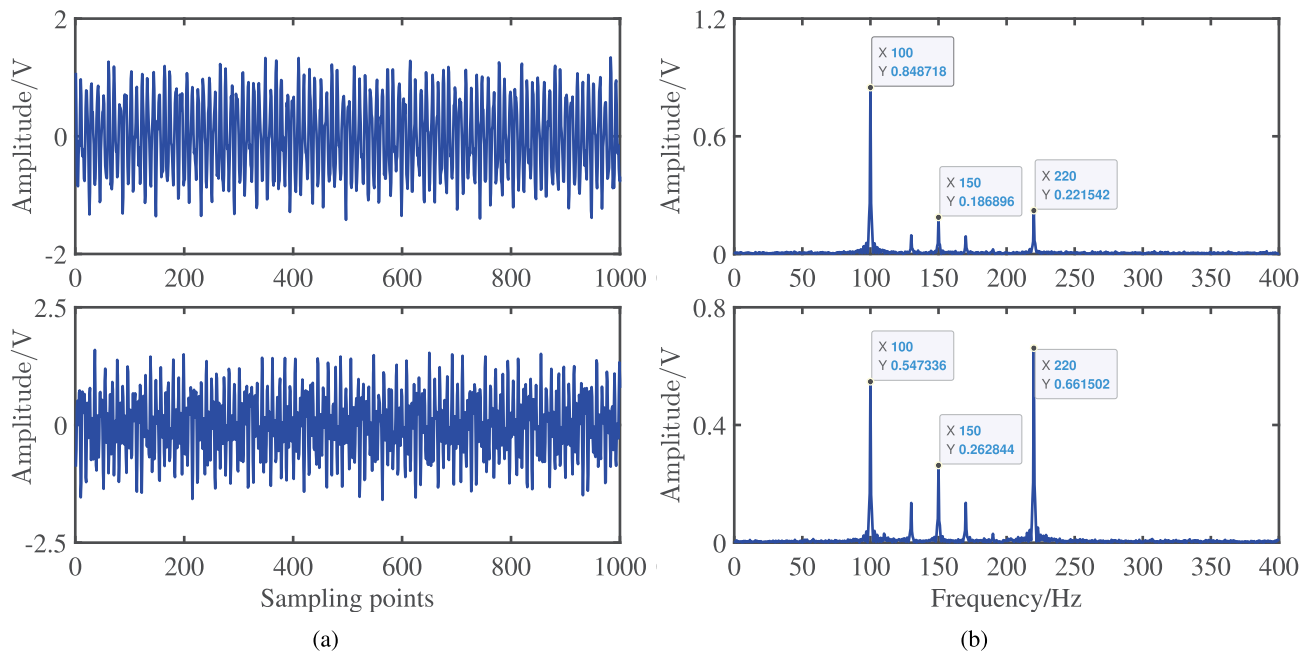**FIGURE 9.** Source signals: (a) Waveforms; (b) Fourier spectrums.

FIGURE 10. Mixed signals: (a) Waveforms; (b) Fourier spectrums.

mixed signals with multiple fault sources, the general method cannot identify fault characteristics.

We first convert the mixed-signal signal by STFT, and the time-frequency signal is shown in Figure 3(a), and the time-frequency signal after SET conversion is shown in Figure 3(b). After the low energy time-frequency points are eliminated and single source detection is performed, the time-frequency points of the time-frequency signals are

normalized as shown in Figure 4(b). The clustering algorithm DPC was used to remove the anomalies, and the clustering center was plotted as shown in Figure 11, which provides three initial clustering centers.

To enhance the assessment of the overall effectiveness of the proposed method, the simulation process is depicted as follows: two algorithmic processes are deployed, each of which is executed 100 times, and the corresponding
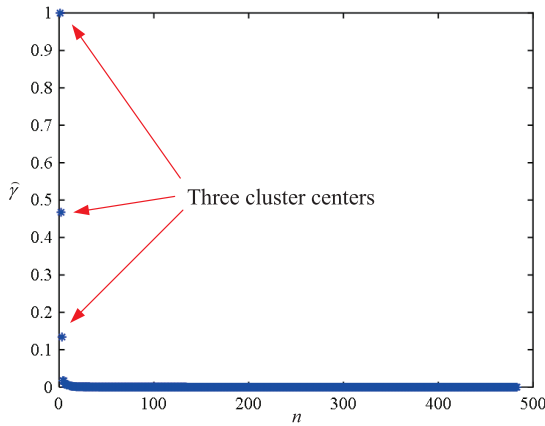
FIGURE 11. The decision graph of IDPC.

100 mixing matrices are calculated using by the underdetermined blind source computational model.

The accuracy of the estimation of the mixing matrix was evaluated using a metric called the normalized mean square error (NMSE), as depicted in (27).

$$NMSE = 10 \lg(\frac{\sum_{i=1}^{m} \sum_{j=1}^{n} (\hat{a}_{ij} - a_{ij})^2}{\sum_{i=1}^{m} \sum_{j=1}^{n} a_{ij}^2}) \quad (27)$$

where m represents the number of columns and n represents the number of rows in mixing matrix $\mathbf{A}$. Furthermore, a_{ij} and $\hat{a}_{ij}$ refer to the elements of mixing matrix $\mathbf{A}$ and the estimated mixing matrix $\hat{\mathbf{A}}$ in the i-th row and j-th column, respectively. It is noteworthy that a smaller NMSE value indicates a more accurate of estimation of the mixing matrix. In other words, the degree of accuracy of estimating the mixing matrix is inversely proportional to the NMSE value. The lower the NMSE value, the more precise is the estimation of the mixing matrix.

Angular deviation is another widely used criterion for evaluation, as shown in Equation (28).

$$ang(a, \hat{a}) = \frac{180}{\pi} \arccos(\frac{\langle a, \hat{a} \rangle}{\|a\| \cdot \|\hat{a}\|}) \quad (28)$$

It measures the degree of overlap between column vectors a and $\hat{a}$ in the corresponding mixing matrix $\mathbf{A}$ and estimated mixing matrix $\hat{\mathbf{A}}$. The angle was converted from radians to degrees using a scaling factor of $180/\pi$. A smaller value for $ang(a, \hat{a})$ implies a greater degree of overlap between vectors, indicating a higher accuracy in estimating the mixing matrix. Table 1 displays the results for the detection angle, whereas Table 2 presents the NMSE values for the mixed matrices.

The first algorithm flow (STFT+Kmeans)

$$\hat{\mathbf{A}}_1 = \begin{bmatrix} -0.8404 & 0.2996 & 0.5778 \\ 0.5397 & -0.9527 & 0.8078 \end{bmatrix} \quad (29)$$

The second algorithm flow (STFT+DPC)

$$\hat{\mathbf{A}}_2 = \begin{bmatrix} -0.8444 & 0.3347 & 0.5865 \\ 0.5356 & -0.9416 & 0.7990 \end{bmatrix} \quad (30)$$

The third algorithm flow (SET+Kmeans)

$$\hat{\mathbf{A}}_3 = \begin{bmatrix} -0.8404 & 0.3146 & 0.5404 \\ 0.5415 & -0.9491 & 0.8406 \end{bmatrix} \quad (31)$$

The forth algorithm flow (STFT+IDPC)

$$\hat{\mathbf{A}}_4 = \begin{bmatrix} -0.8416 & 0.3093 & 0.5605 \\ 0.5353 & -0.9486 & 0.8166 \end{bmatrix} \quad (32)$$

The fifth algorithm flow (SET+DPC)

$$\hat{\mathbf{A}}_5 = \begin{bmatrix} -0.8416 & 0.3093 & 0.5605 \\ 0.5353 & -0.9486 & 0.8166 \end{bmatrix} \quad (33)$$

The sixth algorithm flow (SET+IDPC)

$$\hat{\mathbf{A}}_6 = \begin{bmatrix} -0.8413 & 0.3077 & 0.5628 \\ 0.5395 & -0.9511 & 0.8242 \end{bmatrix} \quad (34)$$

In the Monte Carlo experiment, each computational process was performed 100 times. We observed that for the same method, signal preprocessing using SET outperformed STFT. This superiority was evident in the reduced angular deviation and lower NMSE values (ideal) achieved with SET. When comparing the different methods, the performance of DPC was similar to that of K-means. According to the metrics, both methods exhibited larger angular deviations, and their NMSE values were close, but fell short of the ideal range. For the first five computational processes, the estimated mixing matrices were computed as the mean of 100 runs, as described in Equations (29)-(34). The sixth computational process represents the method used in this study, and the results from 100 runs were consistent, as shown in Equation (34)

From the data in Table 1, we may conclude the following:

(1) The angle deviation of each column vector of the mixed matrix obtained by the STFT + K-means method was the largest, and some values exceeded 5. In this pa- per, the SET + IDPC method is proposed to obtain the minimum angular deviation of each column vector, and they are 0.1080,0.4237,0.6042, respectively, which is much less than that of the other method.

(2) The NMSE values for the STFT+Kmeans algorithm and the SET+Kmeans algorithm are -38.69 and -33.24, respectively. The calculation results did not improve; instead, they deteriorated, indicating the stochastic nature of K-means algorithm because of the arbitrary selection of initial points. For the STFT+DPC algorithm, the NMSE value was -34.05, and for the STFT+IDPC algorithm, it was -41.78. Similarly, for the SET+DPC algorithm, the NMSE was -35.41, and for the SET+IDPC algorithm, it was -42.43. This indicates that IDPC provides more accurate computations than DPC, resulting in significant improvement in the results.

(3) The unpredictable precision of the mixing matrix estimated by the K-means algorithm can be attributed to the random selection of the initial centers in Method 1, where 75% of the estimates are inaccurate, and only 25% yield relatively satisfactory results. These outcomes are considered unacceptable because of their element of chance and the

TABLE 1. Comparisons of angular deviations among different methods.

Method	$ang(\mathbf{a}_1, \hat{\mathbf{a}}_1)$	$ang(\mathbf{a}_2, \hat{\mathbf{a}}_2)$	$ang(\mathbf{a}_3, \hat{\mathbf{a}}_3)$
STFT+Kmeans	2.5704	2.8645	5.9077
STFT+DPC	0.3656	1.2601	1.3821
STFT+IDPC	0.2940	0.2490	0.4331
SET+Kmeans	0.0427	0.0308	2.1622
SET+DPC	0.3074	1.0532	1.1632
SET+IDPC	**0.1080**	**0.4237**	**0.6042**

TABLE 2. Comparisons of the NMSE of different methods.

Method	NMSE	Method	NMSE
STFT+DPC	-34.05	SET+DPC	-35.41
STFT+Kmeans	-38.69	SET+Kmeans	-33.24
STFT+IDPC	-41.78	SET+IDPC	-42.43

TABLE 3. Mechanical specifications of rolling bearings.

Rolling bearing	Size
Inner diameter D_s	0.9843 in
Outside diameter D_m	2.0472 in
Width B	0.5906 in
Nominal diameter D	1.537 in
Spherical diameter d	0.3126 in
Quantity of rolling element Z	9
Contact inclination $\alpha(°)$	0°

TABLE 4. The parameters of the deep groove ball bearings.

Name of each item	Parameter
The diameter of the defect	0.007 in
The motor speed	1797RPM
The load	0 hp
The sampling frequency	12 kHz
The signal length	0.35 s

apparent inconsistency in the results. Additionally, the DPC algorithm exhibits lower computational efficiency and yields larger angular deviations. In contrast, the mixing matrix estimated in the sixth computational process, which is the method utilized in this study, remained constant across 100 iterations, demonstrating the stability and precision of this approach.
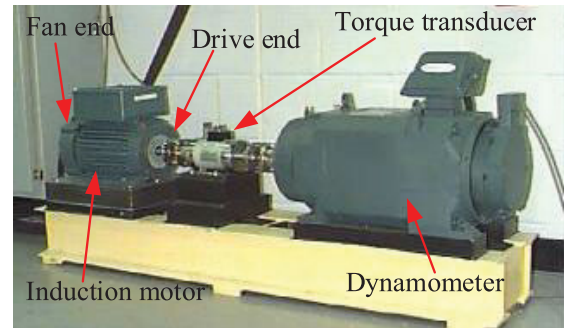
IV. THE EXPERIMENT AND PERFORMANCE ANALYSIS
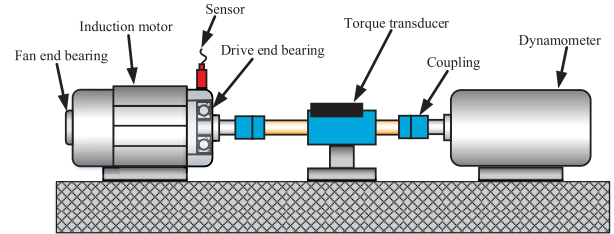
A. EXPERIMENTAL VERIFICATION

This study centers on three distinct sets of experimental bearing data obtained from Western Reserve University in the United States, specifically addressing normal vibration s_1, an inner ring defect s_2, and an outer ring defect s_3. These groups of data were selected as the main research objects for this study. The examined types of bearings are 6205-2RSJEMSKF, which pertain to deep groove ball bearings. The outer and inner rings were manufactured using

TABLE 5. The frequency of the rolling bearing.

Name of each item	Design frequency
The rotational frequency f_r	29.95 Hz
The eigenfrequency of the outer ring f_o	107.4 Hz
The eigenfrequency of the inner ring f_i	162.2 Hz

(a)

(b)

FIGURE 12. CWRU test stands for bearings: (a) test system; (b) test stand structure diagram.

electric discharge machining. The motor drive end has an accelerometer positioned the noon orientation, which enables the acquisition of vibration signals for regular, outer ring and inner ring faults. Figure 12 depicts the bearing test bench and Figure 13 displays the spectra. Table 3 lists the structural parameters of the rolling bearings. The parameters of the deep-groove ball bearings are listed in Table 4. Table 5 presents the frequencies of the rolling bearings.

The rotational frequency f_r of the rolling bearing:

$$f_r = \frac{n}{60} \tag{35}$$

Rolling bearing outer ring failure characteristic frequency f_0:

$$f_o = \frac{1}{2}Z(1 - \frac{d}{D}\cos\alpha)f_r \tag{36}$$

Rolling bearing inner ring failure characteristics frequency f_i:

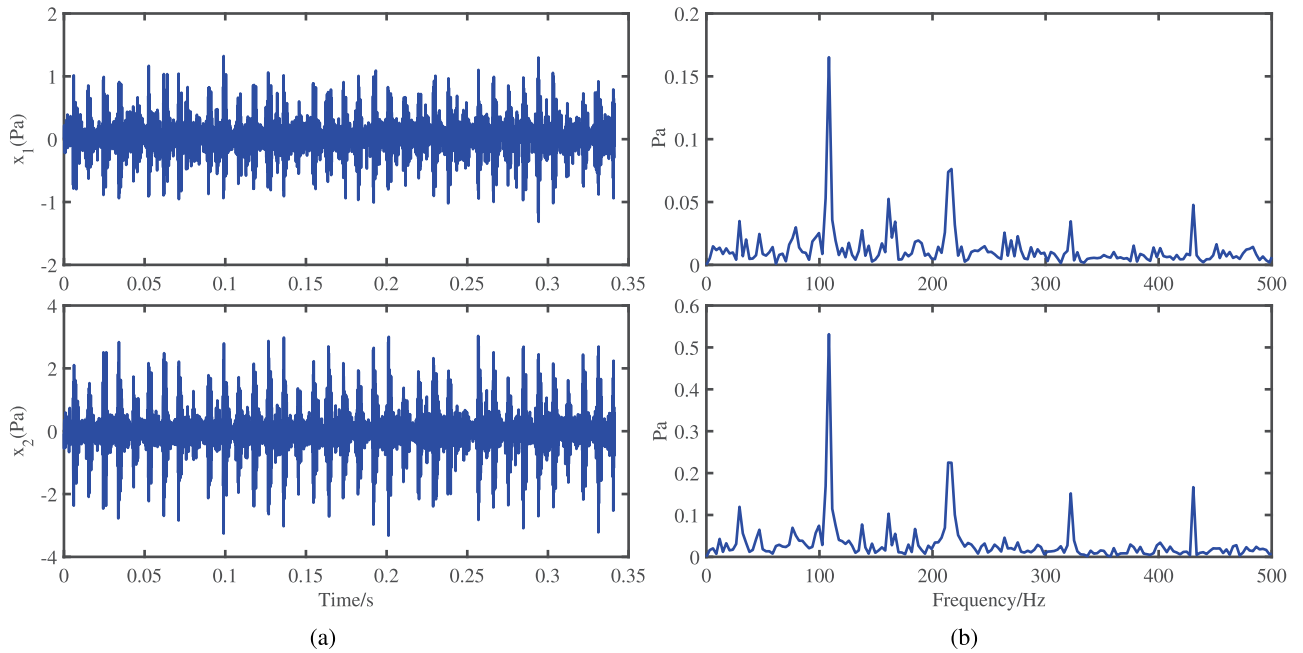$$f_i = \frac{1}{2}Z(1 + \frac{d}{D}\cos\alpha)f_r \tag{37}$$

FIGURE 13. Mixed signals: (a) time domain waveform; (b) frequency Fourier spectrum.
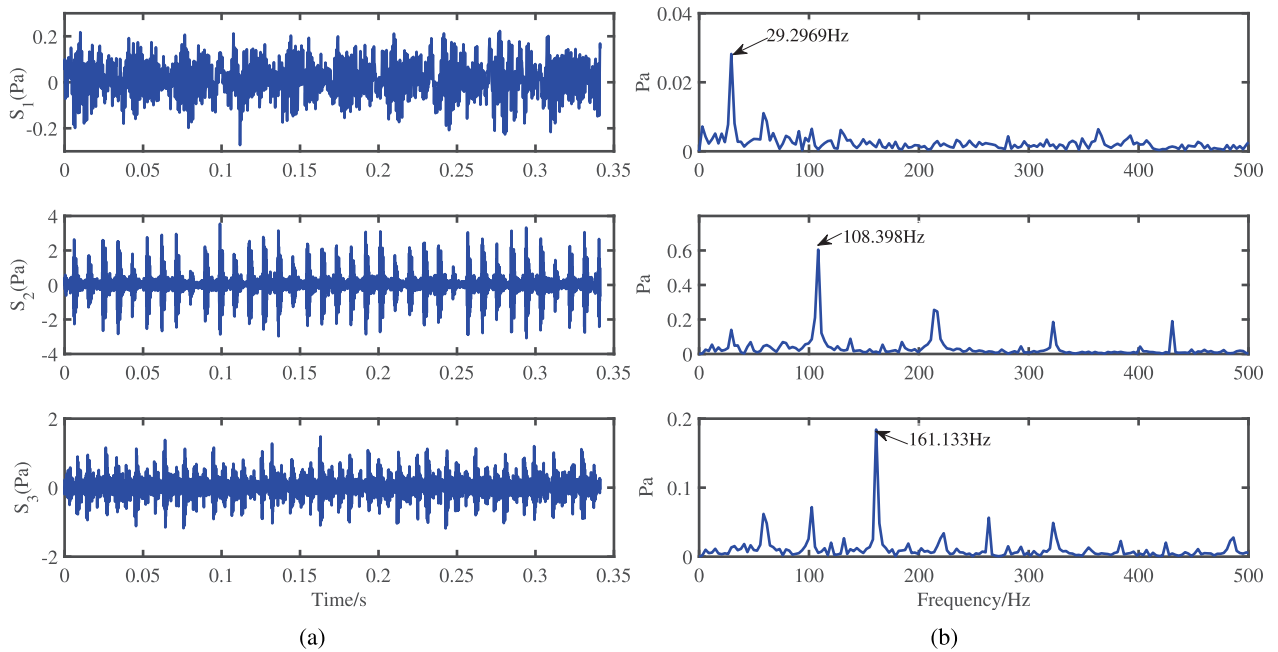

FIGURE 14. Source signals: (a) time domain waveform; (b) frequency Fourier spectrum.

From the mixed signal plot in Figure 13, it is evident that, aside from the prominent first-order outer ring characteristic frequency (f_o) at 108.39Hz and the second-order outer ring frequency at 216.8Hz, the rotational frequency (f_r) at 29.29Hz and the inner ring characteristic frequency (f_i) at 161.13Hz are completely submerged within the noise and are indistinguishable. The time domain plots and envelope spectra of the three source signals are shown in Figure 14, A random matrix is adopted to mix **A**, and the mixing matrix

A is listed in (38):

$$\mathbf{A} = \begin{bmatrix} 0.9848 & 0.3420 & 0.5000 \\ 0.1736 & -0.9397 & 0.8660 \end{bmatrix} \quad (38)$$

B. COMPARISON OF SIX METHODS

As shown in Table 7, we present a comparison between the outcomes obtained using the proposed approach and those obtained using conventional methodologies.
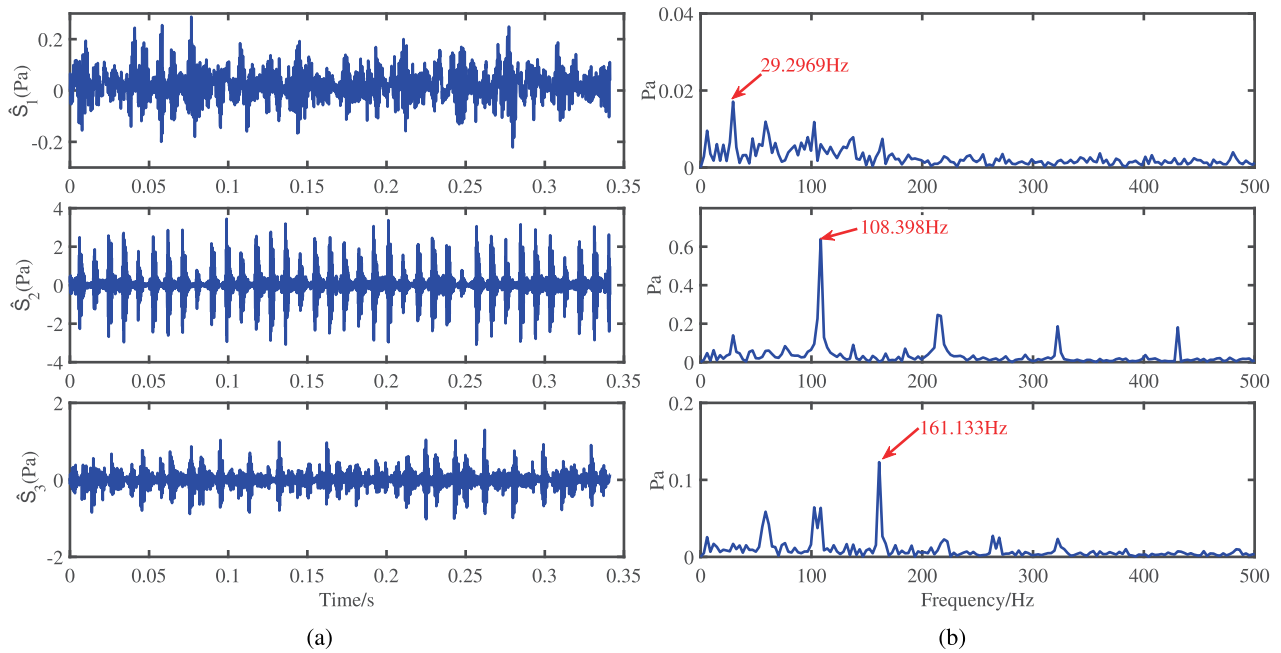
FIGURE 15. Estimated source signals: (a) time domain waveform; (b) frequency Fourier spectrum.

TABLE 6. Comparisons of angular deviations among different methods.

Method	$ang(\mathbf{a}_1, \hat{\mathbf{a}}_1)$	$ang(\mathbf{a}_2, \hat{\mathbf{a}}_2)$	$ang(\mathbf{a}_3, \hat{\mathbf{a}}_3)$
STFT+Kmeans	4.3057	0.8491	7.6080
STFT+DPC	3.1688	1.3583	8.9843
STFT+IDPC	2.9510	0.6481	5.9077
SET+Kmeans	2.0210	0.6246	8.7436
SET+DPC	2.0210	1.1869	9.1886
SET+IDPC	**0.1539**	**0.3674**	**0.9683**

TABLE 7. Comparisons of the NMSE of different methods.

Method	NMSE	Method	NMSE
STFT+DPC	-19.8251	SET+DPC	-20.0374
STFT+Kmeans	-20.3840	SET+Kmeans	-20.1463
STFT+IDPC	-23.2841	SET+IDPC	-35.5926

FIGURE 16. Comparison of estimated source signals with the correlation coefficients.

When comparing the three methods pre-processed by SET with the three methods pre-processed by STFT, it is observed that, by combining SET with other clustering algorithms, the sparsity improves after the time-frequency transformation by SET and performs more robustly than STFT in a noisy environment. When comparing the results of the six methods, it is evident that the approach employed in this study achieved a lower angular deviation and a superior NMSE index. The results of this study indicate that the enhanced methods of sparse representation and sparse component analysis used in this research yielded favorable outcomes, enabling the precise estimation of the mixing matrix.
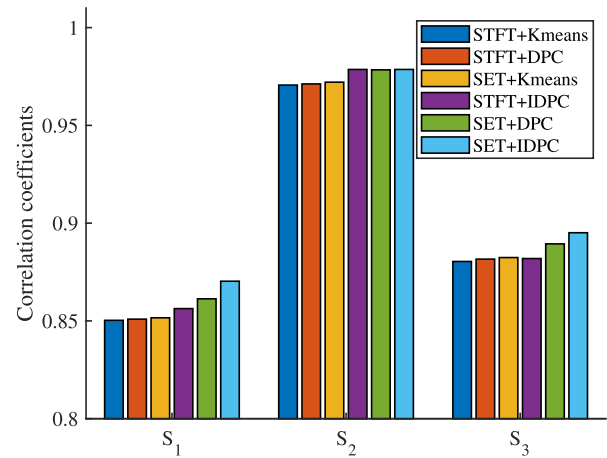
As shown in Figure 14 and 15, the proposed method can recover the shape and frequency characteristics of the source signal in the time domain, which enables an accurate representation of the nonlinear features of non-stationary signals. Similarly, the frequency domain plot of the recovered signal shows that the three eigenfrequencies are 29.2969 Hz, 108.398 and 161.133 Hz, which are in perfect agreement with the experimental eigenfrequencies. Although there was some attenuation in the frequency amplitude, the fault characteristics were presented.

The Pearson correlation coefficient was used to gauge the correlation between the source and estimated signals. As illustrated in Graph 16, it is evident that the method

employed in this study outperformed the other five methods, with the estimated signals closely mirroring the source signals. This substantiates the higher accuracy of the approach used in this study.

V. CONCLUSION

In summary, this study focuses on the adverse effects of vibration and noise caused by mechanical failures, with a particular emphasis on roll-bearing faults. We introduced an effective method for separating and recovering non-stationary and nonlinear complex-coupled signals. Moreover, the identification of fault characteristics was simplified through envelope analysis, thereby enhancing its applicability to mechanical fault diagnosis studies.

Within the framework of sparse component analysis, this study introduces an innovative UBSS approach that combines SET with enhanced DPC and K-means for mixing matrix estimation. SET significantly enhances the sparsity of signals, thereby facilitating the separation of mixed signals. Furthermore, we introduced an improved DPC method, which effectively addresses source number estimation issues and robustly eliminates outliers. This enhancement resulted in a more accurate estimation of the mixing matrix. To identify the cluster centers, we employed K-means clustering, which further refined our source separation process. Source signal recovery was achieved using a shortest-path algorithm. Extensive simulations and experiments validated the effectiveness of this method, surpassing that of traditional techniques.

In this study, we assumed that the source signals propagated linearly to sensors. However, in practical scenarios, various vibration sources can be introduced nonlinearity and signal loss during propagation to sensors. This real-world complexity was not explicitly addressed in this study. Therefore, in future research, we propose exploring a more practical and complex scenario of nonlinear and time-delayed convolutional hybrid models. This finding is of significant practical importance and warrants further investigation.

REFERENCES

[1] Z. Haiyang, W. Jindong, J. Lee, and L. Ying, "A compound interpolation envelope local mean decomposition and its application for fault diagnosis of reciprocating compressors," *Mech. Syst. Signal Process.*, vol. 110, pp. 273–295, Sep. 2018.

[2] A. Holobar and D. Farina, "Noninvasive neural interfacing with wearable muscle sensors: Combining convolutive blind source separation methods and deep learning techniques for neural decoding," *IEEE Signal Process. Mag.*, vol. 38, no. 4, pp. 103–118, Jul. 2021.

[3] F. Miao, R. Zhao, L. Jia, and X. Wang, "Multisource fault signal separation of rotating machinery based on wavelet packet and fast independent component analysis," *Int. J. Rotating Machinery*, vol. 2021, pp. 1–17, May 2021.

[4] B. Lu, "Intelligent control system of physical strength in sports based on independent component analysis," *Neural Comput. Appl.*, vol. 35, no. 6, pp. 4397–4408, Feb. 2023.

[5] M. T. Islam, K. M. Hasib, M. M. Rahman, A. N. Tusher, M. S. Alam, and M. R. Islam, "Convolutional auto-encoder and independent component analysis based automatic place recognition for moving robot in invariant season condition," *Human-Centric Intell. Syst.*, vol. 3, no. 1, pp. 13–24, Dec. 2022.

[6] Z. Yi, N. Pan, and Y. Guo, "Mechanical compound faults extraction based on improved frequency domain blind deconvolution algorithm," *Mech. Syst. Signal Process.*, vol. 113, pp. 180–188, Dec. 2018.

[7] W. Cheng, Z. Jia, X. Chen, and L. Gao, "Convolutive blind source separation in frequency domain with kurtosis maximization by modified conjugate gradient," *Mech. Syst. Signal Process.*, vol. 134, Dec. 2019, Art. no. 106331.

[8] L. Parra and C. Spence, "Convolutive blind separation of non-stationary sources," *IEEE Trans. Speech Audio Process.*, vol. 8, no. 3, pp. 320–327, May 2000.

[9] T. Ding, H. Chen, L. Chen, J. Shi, and Y. Zhou, "Improved sparse component analysis for multi-point harmonic contribution evaluation under incomplete measurements," *IEEE Trans. Power Del.*, vol. 37, no. 5, pp. 4019–4031, Oct. 2022.

[10] J. Wang, X. Chen, H. Zhao, Y. Li, and D. Yu, "An effective two-stage clustering method for mixing matrix estimation in instantaneous underdetermined blind source separation and its application in fault diagnosis," *IEEE Access*, vol. 9, pp. 115256–115269, 2021.

[11] O. Yilmaz and S. Rickard, "Blind separation of speech mixtures via time-frequency masking," *IEEE Trans. Signal Process.*, vol. 52, no. 7, pp. 1830–1847, Jul. 2004.

[12] F. Abrard and Y. Deville, "A time–frequency blind signal separation method applicable to underdetermined mixtures of dependent sources," *Signal Process.*, vol. 85, no. 7, pp. 1389–1403, Jul. 2005.

[13] Y. Deville and M. Puigt, "Temporal and time-frequency correlation-based blind source separation methods. Part I: Determined and underdetermined linear instantaneous mixtures," *Signal Process.*, vol. 87, no. 3, pp. 374–407, Mar. 2007.

[14] S. Arberet, R. Gribonval, and F. Bimbot, "A robust method to count and locate audio sources in a multichannel underdetermined mixture," *IEEE Trans. Signal Process.*, vol. 58, no. 1, pp. 121–133, Jan. 2010.

[15] A. Aissa-El-Bey, N. Linh-Trung, K. Abed-Meraim, A. Belouchrani, and Y. Grenier, "Underdetermined blind separation of nondisjoint sources in the time-frequency domain," *IEEE Trans. Signal Process.*, vol. 55, no. 3, pp. 897–907, Mar. 2007.

[16] F. M. Naini, G. H. Mohimani, M. Babaie-Zadeh, and C. Jutten, "Estimating the mixing matrix in sparse component analysis (SCA) based on partial k-dimensional subspace clustering," *Neurocomputing*, vol. 71, nos. 10–12, pp. 2330–2343, Jun. 2008.

[17] V. G. Reju, S. N. Koh, and I. Y. Soon, "An algorithm for mixing matrix estimation in instantaneous blind source separation," *Signal Process.*, vol. 89, no. 9, pp. 1762–1773, Sep. 2009.

[18] V. G. Reju, S. Nqee Koh, and I. Yann Soon, "Underdetermined convolutive blind source separation via time–frequency masking," *IEEE Trans. Audio, Speech, Language Process.*, vol. 18, no. 1, pp. 101–116, Jan. 2010.

[19] W. Bao, F. Li, X. Tu, Y. Hu, and Z. He, "Second-order synchroextracting transform with application to fault diagnosis," *IEEE Trans. Instrum. Meas.*, vol. 70, pp. 1–9, 2021.

[20] Y. Tian, J. Gao, and D. Wang, "Synchrosqueezing optimal basic wavelet transform and its application on sedimentary cycle division," *IEEE Trans. Geosci. Remote Sens.*, vol. 60, 2022, Art. no. 5908413.

[21] M. Puigt, A. Griffin, and A. Mouchtaris, "Nonlinear blind mixture identification using local source sparsity and functional data clustering," in *Proc. IEEE 7th Sensor Array Multichannel Signal Process. Workshop (SAM)*, Jun. 2012, pp. 481–484.

[22] D. Pavlidi, A. Griffin, M. Puigt, and A. Mouchtaris, "Real-time multiple sound source localization and counting using a circular microphone array," *IEEE Trans. Audio, Speech, Language Process.*, vol. 21, pp. 2193–2206, 2013.

[23] M. S. Karoui, Y. Deville, S. Hosseini, and A. Ouamri, "Blind spatial unmixing of multispectral images: New methods combining sparse component analysis, clustering and non-negativity constraints," *Pattern Recognit.*, vol. 45, no. 12, pp. 4263–4278, Dec. 2012.

[24] X. Fu, W.-K. Ma, K. Huang, and N. D. Sidiropoulos, "Blind separation of quasi-stationary sources: Exploiting convex geometry in covariance domain," *IEEE Trans. Signal Process.*, vol. 63, no. 9, pp. 2306–2320, May 2015.

[25] K. Abbas, M. Puigt, G. Delmaire, and G. Roussel, "Joint unmixing and demosaicing methods for snapshot spectral images," in *Proc. ICASSP - IEEE Int. Conf. Acoust., Speech Signal Process. (ICASSP)*, Jun. 2023, pp. 1–5.

[26] J. Yao, Y. Xiang, S. Qian, S. Wang, and S. Wu, "Noise source identification of diesel engine based on variational mode decomposition and robust independent component analysis," *Appl. Acoust.*, vol. 116, pp. 184–194, Jan. 2017.

[27] A. Rodriguez and A. Laio, "Clustering by fast search and find of density peaks," *Science*, vol. 344, no. 6191, pp. 1492–1496, Jun. 2014.

[28] X. L. Xie and G. Beni, "A validity measure for fuzzy clustering," *IEEE Trans. Pattern Anal. Mach. Intell.*, vol. 13, no. 8, pp. 841–847, Aug. 1991.

[29] D. Feng and C. K. Tse, "Shape-based image retrieval by shape contexts," *IEEE Trans. Image Process.*, vol. 14, no. 9, pp. 1423–1436, Sep. 2005.

[30] H. Jun, Y. Chen, Q.-H. Zhang, G. Sun, and Q. Hu, "Blind source separation method for bearing vibration signals," *IEEE Access*, vol. 6, pp. 658–664, 2018.

[31] S. Wei, F. Wang, and D. Jiang, "Sparse component analysis based on an improved ant K-means clustering algorithm for underdetermined blind source separation," in *Proc. IEEE 16th Int. Conf. Netw., Sens. Control (ICNSC)*, May 2019, doi: 10.1109/ICNSC.2019.8743171.

[32] S. Askari, "Fuzzy C-means clustering algorithm for data with unequal cluster sizes and contaminated with noise and outliers: Review and development," *Expert Syst. Appl.*, vol. 165, Mar. 2021, Art. no. 113856.

[33] T. Sgouros and N. Mitianoudis, "A novel directional framework for source counting and source separation in instantaneous underdetermined audio mixtures," *IEEE/ACM Trans. Audio, Speech, Language Process.*, vol. 28, pp. 2025–2035, Jun. 2020.

[34] S. Qian and D. Chen, "Joint timefrequency analysis," *IEEE Signal Process. Mag.*, vol. 16, no. 2, pp. 52–67, Mar. 1999.

[35] I. Daubechies, J. Lu, and H.-T. Wu, "Synchrosqueezed wavelet transforms: An empirical mode decomposition-like tool," *Appl. Comput. Harmon. Anal.*, vol. 30, no. 2, pp. 243–261, Mar. 2011.

[36] S. Wang, X. Chen, G. Cai, B. Chen, X. Li, and Z. He, "Matching demodulation transform and SynchroSqueezing in time-frequency analysis," *IEEE Trans. Signal Process.*, vol. 62, no. 1, pp. 69–84, Jan. 2014.

[37] T. Oberlin, S. Meignen, and V. Perrier, "Second-order synchrosqueezing transform or invertible reassignment? Towards ideal time-frequency representations," *IEEE Trans. Signal Process.*, vol. 63, no. 5, pp. 1335–1344, Mar. 2015.

[38] M. Yu, C. Xu, and C. Xu, "Synchroextracting transform," *IEEE Trans. Ind. Electron.*, vol. 63, no. 5, pp. 8042–8054, Mar. 2016.

[39] J. Lu, W. Cheng, D. He, and Y. Zi, "A novel underdetermined blind source separation method with noise and unknown source number," *J. Sound Vibrat.*, vol. 457, pp. 67–91, Sep. 2019.

[40] Y. Wang, D. Wang, W. Pang, C. Miao, A.-H. Tan, and Y. Zhou, "A systematic density-based clustering method using anchor points," *Neurocomputing*, vol. 400, pp. 352–370, Aug. 2020.

[41] M. Du, S. Ding, and H. Jia, "Study on density peaks clustering based on k-nearest neighbors and principal component analysis," *Knowl.-Based Syst.*, vol. 99, pp. 135–145, May 2016.

[42] J. Lu, W. Cheng, and Y. Zi, "A novel underdetermined blind source separation method and its application to source contribution quantitative estimation," *Sensors*, vol. 19, no. 6, p. 1413, Mar. 2019.

[43] X. Xu, S. Ding, and Z. Shi, "An improved density peaks clustering algorithm with fast finding cluster centers," *Knowl.-Based Syst.*, vol. 158, pp. 65–74, Oct. 2018.

[44] J. Hou, A. Zhang, and N. Qi, "Density peak clustering based on relative density relationship," *Pattern Recognit.*, vol. 108, Dec. 2020, Art. no. 107554.

[45] K. G. Flores and S. E. Garza, "Density peak clustering with gap-based automatic center detection," *Knowl.-Based Syst.*, vol. 206, Oct. 2020, Art. no. 106350.

[46] X. Xu, S. Ding, H. Xu, H. Liao, and Y. Xue, "A feasible density peaks clustering algorithm with a merging strategy," *Soft Comput.*, vol. 23, no. 13, pp. 5171–5183, Jul. 2019.

[47] K. M. Kumar and A. R. M. Reddy, "An efficient k-means clustering filtering algorithm using density based initial cluster centers," *Inf. Sci.*, vols. 418–419, pp. 286–301, Dec. 2017.

[48] R. Capor Hrosik, E. Tuba, E. Dolicanin, R. Jovanovic, and M. Tuba, "Brain image segmentation based on firefly algorithm combined with K-means clustering," *Stud. Informat. Control*, vol. 28, no. 2, pp. 167–176, Jul. 2019.

YANYANG LI received the M.S. degree from the School of Astronautics, Harbin Institute of Technology, Harbin, China, in 2005. She is currently pursuing the Ph.D. degree with the College of Mechanical Science and Engineering, Northeast Petroleum University, Daqing. Her research interests include fault diagnosis, blind source separation, and dynamics.

JINDONG WANG received the B.S. and M.S. degrees from the College of Mechanical Science and Engineering, Northeast Petroleum University, Daqing, China, in 1986 and 1989, respectively, and the Ph.D. degree from the School of Mechanical Science and Engineering, Dalian University of Technology, Dalian, China, in 2000. He is currently a Professor with the College of Mechanical Science and Engineering, Northeast Petroleum University. His research interests include control, dynamics, and signal processing.

HAIYANG ZHAO received the Ph.D. degree from the School of Astronautics, Harbin Institute of Technology, Harbin, China, in 2014. He is currently an Associate Professor with the College of Mechanical Science and Engineering, Northeast Petroleum University. His research interests include mechanical dynamics, fault diagnosis, and signal processing.

CHANG WANG was born in China, in 1995. He is currently pursuing the M.S. degree with the College of Mechanical Science and Engineering, Northeast Petroleum University, Daqing. His research interests include fault diagnosis and blind source separation.

ZHICHAO MA was born in China, in 1998. He received the B.S. degree from the School of Mechanical, Electronic, and Control Engineering, Beijing Jiaotong University, in 2021. He is currently pursuing the M.S. degree from the College of Mechanical Science and Engineering, Northeast Petroleum University, Daqing. His research interests include fault diagnosis and blind source separation.

● ● ●